Synthesis, Characterization of g-C$_3$N$_4$/SrTiO$_3$ Heterojunctions and Photocatalytic Activity for Organic Pollutants Degradation

Panagiotis-Spyridon Konstas, Ioannis Konstantinou *, Dimitrios Petrakis and Triantafyllos Albanis *

Department of Chemistry, University of Ioannina, 45110 Ioannina, Greece; pkonstas@cc.uoi.gr (P.-S.K.); dpetrakis@uoi.gr (D.P.)

* Correspondence: iokonst@cc.uoi.gr (I.K.); talbanis@uoi.gr (T.A.); Tel.: +30-26510-08349 (I.K.); +30-26510-08348 (T.A.)

check for updates

Abstract: Perovskite-structure SrTiO$_3$ (STO) and graphitic carbon nitride (g-C$_3$N$_4$, CN) have attracted considerable attention in photocatalytic technology due to their unique properties, but also suffer from some drawbacks. The development of composite photocatalysts that combine properties of the individual semiconductors with enhanced charge separation is the current major trend in the photocatalysis field. In this study, SrTiO$_3$/g-C$_3$N$_4$ (CNSTO) composites with different ratios (10, 20, 30, 40 and 50% g-C$_3$N$_4$) were prepared with a sonication mixing method. The samples were characterized by X-ray diffraction (XRD), scanning electron microscopy (SEM), N$_2$ porosimetry, Fourrier transform infra-red spectroscopy (FT-IR), UV-Vis diffuse reflectance (DRS) and dynamic light scattering (DLS). STO spherical particles were successfully loaded on the g-C$_3$N$_4$ planes forming heterojunction composite materials. The photocatalytic activity was tested against the degradation of methylene blue (MB) dye under simulated solar light (SSL) irradiation following first-order kinetics. The photocatalytic activity followed the trend: 20CNSTO > 30CNSTO > 40CNSTO > 50CNSTO ≈ 10CNSTO, in accordance with the amount of •OH radicals determined by fluorescence spectroscopy. A Z-scheme mechanism was proposed for the enhanced photocatalytic degradation of MB as evidenced by trapping experiments with scavengers. Finally, significant stability and reusability was exhibited, indicating that such composites are of potential interest for photocatalytic treatments under sunlight irradiation.

Keywords: g-C$_3$N$_4$/SrTiO$_3$; composites; heterojunction; photocatalysis; Z-scheme

1. Introduction

Photocatalysis with semiconductors is an advanced oxidation process for organic pollution abatement that has received great interest due to several advantages, such as the use of ambient conditions of temperature and pressure, the use of solar light, the absence of fouling, lack of mass transfer limitation, and the mineralization of organic pollutants into carbon dioxide, water and inorganic ions [1–4].

Titanate perovskites, ATiO$_3$ (A = Ca, Sr, Ba, etc.), are semiconductors with a wide band gap and interesting electronic, optical, magnetic and photocatalytic properties. They are considered promising materials for photocatalytic processes because of their strong resistance to photo corrosion, suitable oxidation potential and their high physicochemical stability [5–8]. Among them, SrTiO$_3$ is the most promising material for photocatalytic applications [9–12]. It is a cubic perovskite (Pm3m, a = 3.9 Å) n-type semiconductor with an indirect band gap of 3.1–3.7 eV depending on the crystal structure and

morphology obtained by the synthesis method [13,14]. Therefore, $SrTiO_3$ is an excellent photocatalyst only under UV light, which include about 5.0% of sunlight energy [15]. Modification of $SrTiO_3$ in order to increase absorptivity into the visible light spectrum has been mainly studied by transition metal doping of the Ti site [16] and by noble metals deposition on the semiconductor surface [17]. However, the use of rare or precious metals constitutes an important disadvantage [18]. Because of this, non-metal doping [19] and coupling with other semiconductors like TiO_2 [20] and $ZnFe_2O_4$ [21] are considered effective alternative methods to increase the activity.

On the other hand, graphitic carbon nitride (g-C_3N_4) is a polymeric semiconductor with a mild band gap (2.7 eV) and a good response to visible light (up to 460 nm). The medium band gap, along with low cost, simple preparation method, high chemical stability, and non-toxicity, makes g-C_3N_4 appropriate for photocatalytic applications, including organic pollutant degradation, water splitting, CO_2 reduction and organic synthesis under visible light [22–26]. In addition, g-C_3N_4 has found application in optical and electronic devices, chemical sensors, and energy generation/storage [23,27–33].

Despite its remarkable electronic and optical properties, g-C_3N_4 photocatalytic activity faces some limitations, such as the high recombination of charge carriers, low conductivity, low valence band (VB) potential and small specific surface area (<10 m^2 g^{-1}) [34–38]. Methods that have been used so far to increase the photocatalytic activity of g-C_3N_4 include metal and non-metal doping [39–42] and the application of g-C_3N_4 as a sensitizer with well-known photocatalysts like TiO_2 [43] and TaON [44]. In the last few years g-C_3N_4 has been widely used in formation of heterojunctions with perovskites in order to improve their photocatalytic performance. Heterojunctions are mainly formed by g-C_3N_4 and $LaTiO_3$/N-$LaTiO_3$ [45], $LaFeO_3$ [46], $CaTiO_3$ [47], N-doped $SrTiO_3$ [48] and the layered perovskite oxide La_2NiO_4 [49]. However, only a couple of reports have been made on the synthesis and applications of g-C_3N_4/$SrTiO_3$ heterojunctions for oxidation of pollutants, and in general, only low loading ratios have been examined. For example, Cr-doped and N-doped $SrTiO_3$/g-C_3N_4 have been studied for environmental remediation under solar and visible light [48,50]. On the other hand, g-C_3N_4/$SrTiO_3$ and g-C_3N_4/$SrTiO_3$: Rh heterostructures have been studied for photocatalytic H_2 evolution [51,52].

Based on the previous statements, the principal aims of this study are: (i) the preparation of a series of heterojunctions $SrTiO_3$/g-C_3N_4 with different ratios of g-C_3N_4, as very few reports have been made regarding their applications in pollutant oxidation; (ii) the characterization of the prepared photocatalysts with a variety of techniques in order to understand the components with respect to their photocatalytic activity; and (iii) the study of their photocatalytic activity towards the degradation of organic pollutants in aqueous phase using methylene blue (MB) dye as a model compound and $^{\bullet}$OH radicals formation by fluorescence measurements.

2. Results and Discussion

2.1. Characterization of the Prepared Photocatalysts

2.1.1. XRD Analysis

The XRD patterns (Figure 1) of all the prepared g-C_3N_4/$SrTiO_3$ photocatalysts were assigned to $SrTiO_3$ perovskite phase with cubic symmetry (JCPDS no. 79-0176). The main peaks, at about 32.4°, 39.9°, 46.4°, 57.8°, 67.8° and 77.2°, represent the $SrTiO_3$ (1 1 0), (1 1 1), (2 0 0), (2 1 1), (2 2 0) and (3 1 0) surfaces, respectively. The XRD pattern of g-C_3N_4 with hexagonal symmetry is also presented in Figure 1 (JCPDS no. 87-1526). The weak peak at 13.1° (110) and the strong one at 27.4° (200) represent the g-C_3N_4 surfaces. The sharp peaks in all patterns indicate that the obtained powders are highly crystalline, and that they have no impurities. The XRD data was performed by Rietveld refinement, as reported in [53]. The crystal size of all the materials was calculated by appropriate software, using a Williamson and Hull [54–56]-type plotting method, and ranged from 17.1 nm for the 10CNSTO to 29.0 nm for the 30CNSTO, as shown in Table 1. The refinement parameters of % crystal phase, cell parameters (a, b and c), strain analysis and R^2 are also presented in Table 1. The lattice constants (a,

b, c) of SrTiO$_3$ in the composites are slightly higher than those of pure SrTiO$_3$. It can be observed that the crystal size values of the materials present a small variation, increasing along with the % content of CN until 30CNSTO, and then they decrease. In the composites 40CNSTO and 50CNSTO, the peak at 27.4° that corresponds to g-C$_3$N$_4$ is hardly observed. This is because g-C$_3$N$_4$ is partly exfoliated in the mixing process by sonication. As a result, lamellar structure of g-C$_3$N$_4$ was formed and so the crystallization degree is limited. The same observation has been reported in other studies, too [57,58]. In the rest of the materials, the diffraction peaks did not change after the introduction of g-C$_3$N$_4$. Hydrodynamic particle size (median diameter) measurements were also performed by the dynamic light scattering (DLS) and the values ranged from 0.302 μm for the CN to 0.345 μm for the STO, indicating the formation of aggregates in aqueous solutions.
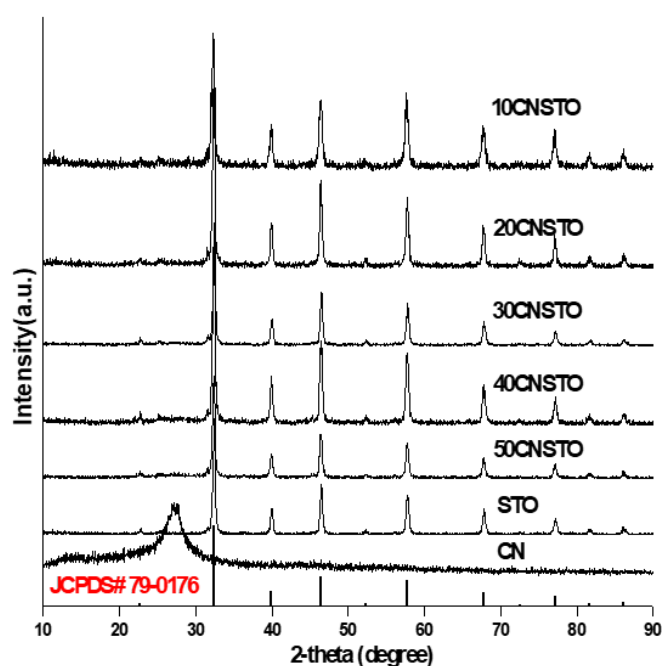

**Figure 1.** XRD patterns of the prepared heterojunctions in comparison with STO.

Table 1. XRD results and Rietveld analysis of all photocatalysts.

| Code Name	Crystal Phase	Space Group	% Phase	a	b	c	Unit Cell Volume (A^3)	E %	R %	Crystal Size (nm)	% Strain	R^2
10CNSTO	SrTiO$_3$	cubic	100	3.9114	3.9114	3.9114	59.84	19.16	26.87	17.1	−0.074	−0.359
20CNSTO	SrTiO$_3$	cubic	100	3.9104	3.9105	3.9105	59.80	16.16	23.53	25.5	−0.037	−0.320
30CNSTO	SrTiO$_3$	cubic	100	3.9093	3.9093	3.9093	59.74	13.77	21.22	29.0	0.000	0.060
40CNSTO	SrTiO$_3$	cubic	100	3.9099	3.9099	3.9099	59.77	16.00	24.99	24.9	−0.005	−0.106
50CNSTO	SrTiO$_3$	cubic	100	3.9103	3.9103	3.9103	59.79	16.04	25.29	24.2	−0.040	−0.332
STO	SrTiO$_3$	cubic	100	3.9087	3.9087	3.9087	59.7	14.79	20.62	27.5	0.016	0.930

2.1.2. Morphology—Surface Analysis of the Photocatalysts

Representative nitrogen adsorption–desorption isotherms of the 10CNSTO and the 20CNSTO catalysts are presented in Figure 2. The photocatalysts are non-porous materials and the isotherms belong to type II, according to IUPAC classification [59]. Their specific surface areas (SSA) are 29.6 and 32.3 m^2/g, respectively. Representative SEM images of CN, STO and 20CNSTO, 30CNSTO are shown in Figure 3. CN (Figure 3a) presented some sheet layers and sheet stacks with a smooth surface and irregular shape. The SEM image of STO (Figure 3b) clearly revealed spherical particles. The images of 20CNSTO and 30CNSTO (Figure 3c,d) showed that, after mixing with g-C$_3$N$_4$, the spherical particles of SrTiO$_3$ were deposited in the CN sheet-stacks.

The PZC (Point of Zero Charge) values of STO and CN were determined to be 9.33 and 4.63, respectively. 10CNSTO, 20CNSTO, 30CNSTO, 40CNSTO and 50CNSTO presented PZC values 8.02, 7.90, 7.87, 7.79 and 7.65 respectively. It is observed that the increment of CN decreases the PZC of the composite materials.


(a)　　　　　　　　　　　　　　　　　　　　　　　　(b)
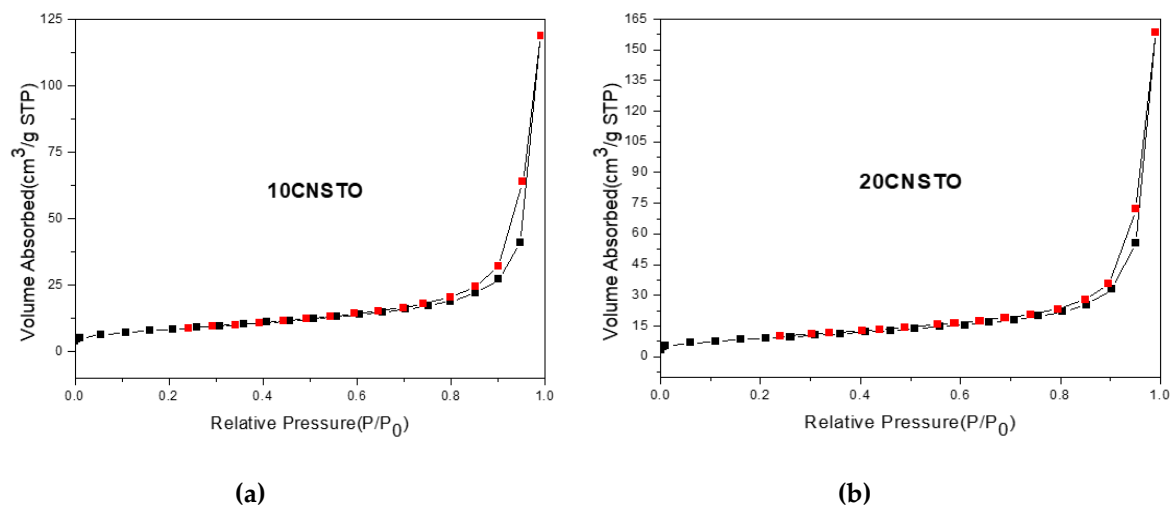
Figure 2. Adsorption–desorption isotherms for 10CNSTO (**a**)and 20CNSTO (**b**) composites.
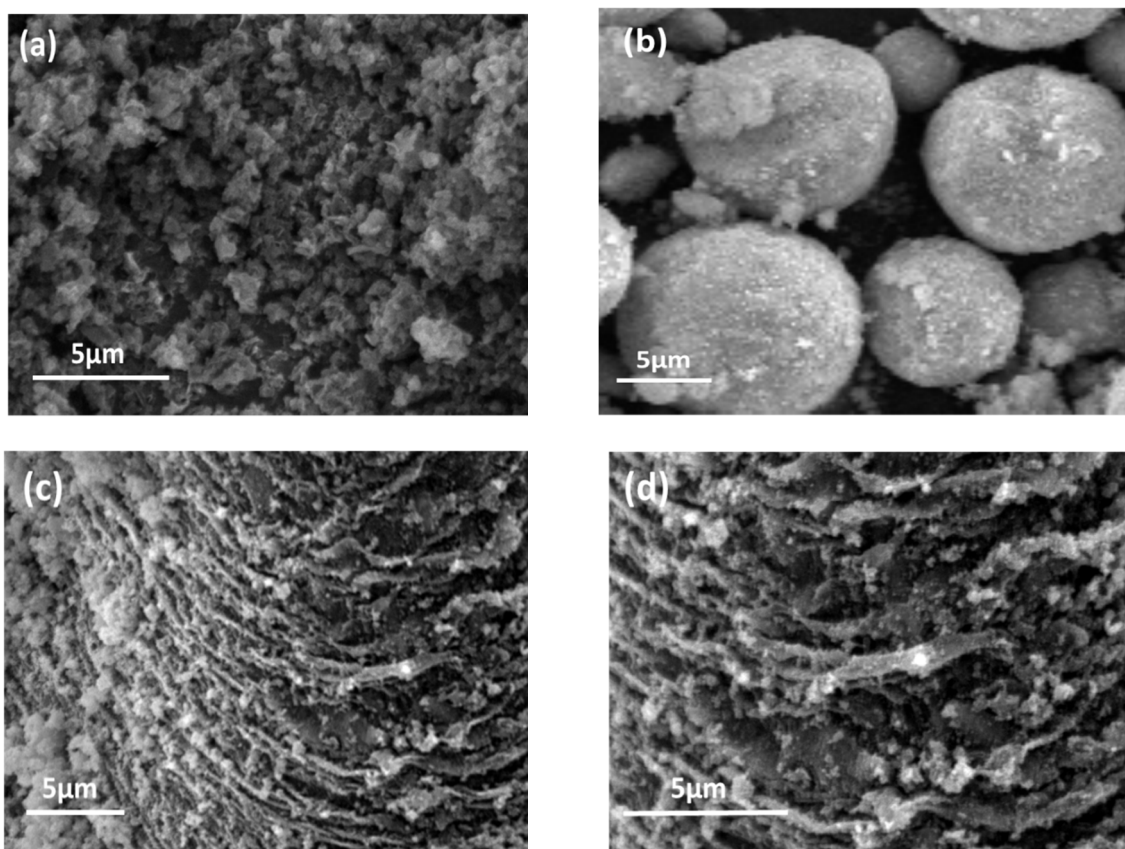
Figure 3. Representative SEM images of the photocatalysts: (**a**) CN (magnification ×3000); (**b**) STO (magnification ×2000); (**c**) 20CNSTO(magnification ×3000); and (**d**) 30CNSTO (magnification ×5000).

2.1.3. FT-IR Spectroscopy

The FT-IR spectra of the g-C_3N_4/$SrTiO_3$ photocatalysts, CN and STO are presented in Figure 4. In all samples except CN, the shoulder below 1000 cm^{-1} appears because of the $SrTiO_3$ crystal lattice vibrations [60]. Bands at around 858 and 596 cm^{-1} are caused by the stretching vibration of the Sr–O and Ti–O bonds, respectively [61]. The band at 1637 cm^{-1} for STO is due to the bending vibration of –OH (caused by bending water) [60,62]. The absorption peak at around 3443–3447 cm^{-1} could be caused by the stretching vibrations of lattice hydroxyls from Ti–OH, perturbed by nearby Sr atoms or by Sr–OH [60]. For CN, the peak at around 815 cm^{-1} can be attributed to the s-triazine ring vibrations. The observed peaks in the range of 1253–1636 cm^{-1} can be ascribed to the stretching vibrations of aromatic C–N and C≡N in the heterocycles [45]. The peak at around 2173 cm^{-1} is assigned to cyano group stretch, which can be attributed to loss of ammonia [62]. The broad peak at 3180–3340 cm^{-1} can be ascribed to stretching vibration N-H or N=H from uncondensed amine groups [45]. The above-mentioned characteristic peaks of CN and STO are present in the composite materials. The observed shifts of characteristic peaks of g-C_3N_4 in the range of 1253–1636 cm^{-1} for the composite materials indicate the weaker bond strengths of C=N and C–N, and reveal the existence of interactions between g-C_3N_4 and STO. Similarly, shifts in STO characteristic peaks at 584 and 3432 cm^{-1} were observed.
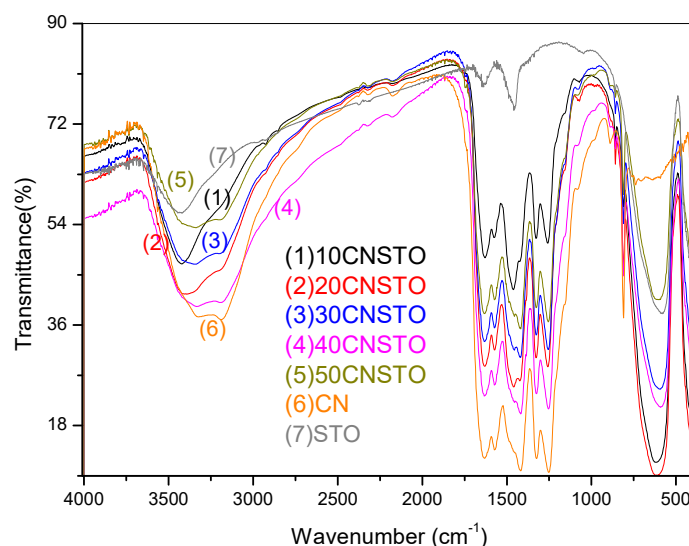
Figure 4. FT-IR spectra of the composite photocatalysts and pristine CN, STO.

2.1.4. UV-Vis Spectra

The diffuse reflectance spectroscopy (DRS) results for all photocatalysts are presented in Figure 5a. The absorption edge of pure $SrTiO_3$ (STO) was about 390–395 nm, as expected, so no response to visible irradiation was observed. On the contrary, the absorption edge of g-C_3N_4 was about 445 nm, indicating visible light response. The E_g values (Table 2) of the photocatalysts were calculated with the use of Kubelka-Munk plots, which are presented in Figure 5b. The Kubelka –Munk plot of 20CNSTO is presented separately in Figure 5c. In both DRS and Kubelka-Munk plots of each photocatalyst, it can be observed that there are bands of both CN and STO. Also, it can be observed that, with the increment of CN in the composites, the band of STO decreases, while the band of CN increases. All the composite samples displayed a significantly enhanced visible light absorption compared to pristine STO.
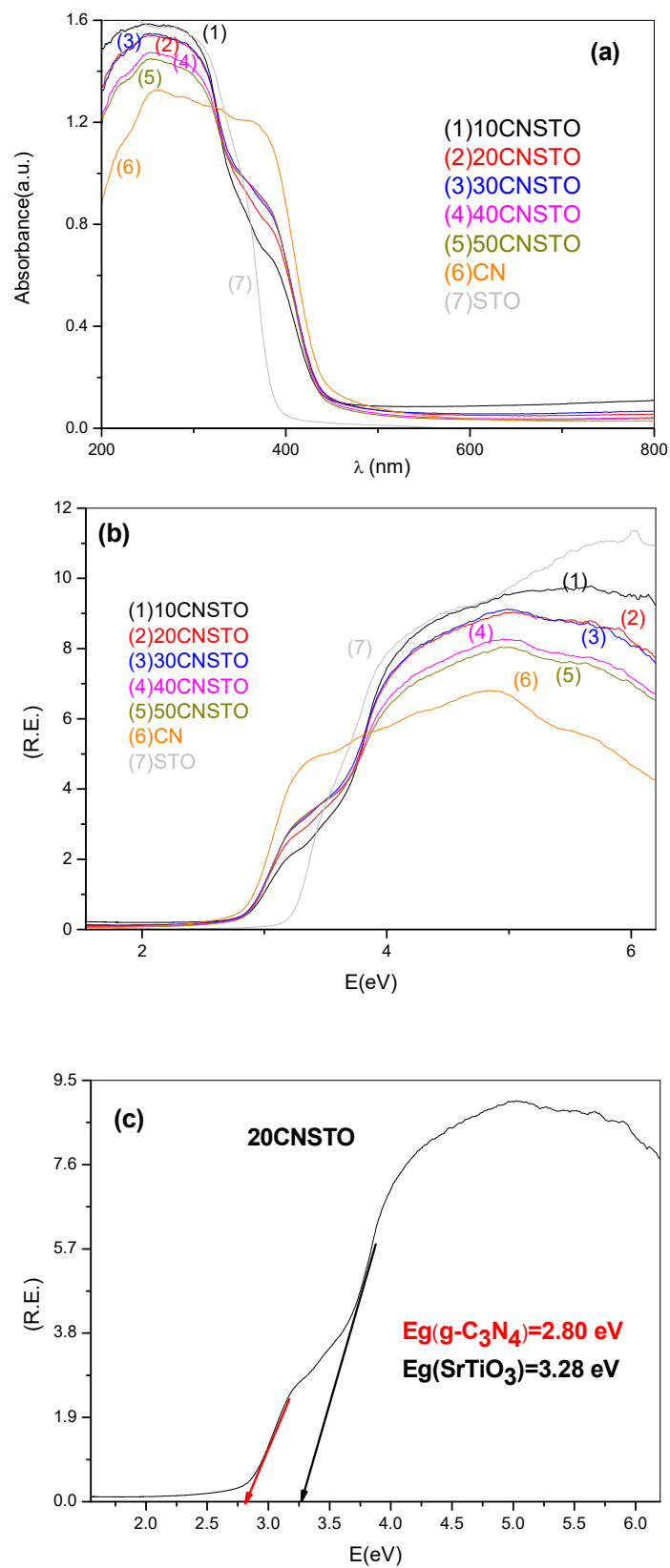
Figure 5. (**a**) DR UV-Vis spectra plots; (**b**) Kubelka-Munk plots for the prepared heterojunctions. R: absorbance, E = 1239.7/λ, energy in eV, λ = wavelength in nm, (**c**) Kubelka-Munk plot for the 20CNSTO heterojunction.

Table 2. Point of zero charge and E_g values of all photocatalysts.

Catalysts	PZC	E_g (eV)	
		g-C_3N_4	$SrTiO_3$
10CNSTO	8.02	2.80	3.40
20CNSTO	7.90	2.80	3.28
30CNSTO	7.87	2.82	3.28
40CNSTO	7.79	2.84	3.20
50CNSTO	7.65	2.84	3.21
CN	4.63	2.82	
STO	9.33		3.15

2.1.5. Determination of $^\bullet$OH by Fluorescence Measurements

The evolution of fluorescence spectra intensity of 2-hydroxyterephthalic acid (OHTA) for the 20CNSTO photocatalyst at different intervals within an irradiation time framework of 120 min is displayed in Figure 6 as a representative example. It can be seen that the fluorescence intensity increases along with irradiation time. The kinetics of $^\bullet$OH radicals formation for all photocatalysts are shown in Figure 7. The ability of the photocatalysts to generate $^\bullet$OH radicals follows the trend: 20CNSTO > 50CNSTO > 30CNSTO > 10CNSTO > 40CNSTO. The 20CNSTO material showed greater $^\bullet$OH formation ability compared to all other prepared composites, which is consistent with the photocatalytic kinetics described in the next paragraph. Thus, it was considered the optimum ratio for such composites.
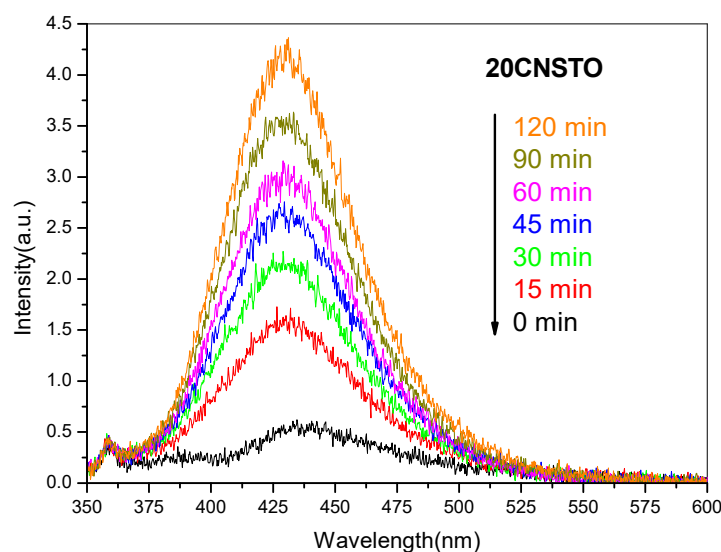
Figure 6. Evolution of OH-TA fluorescence spectra after 120 min of irradiation of 20CNSTO.
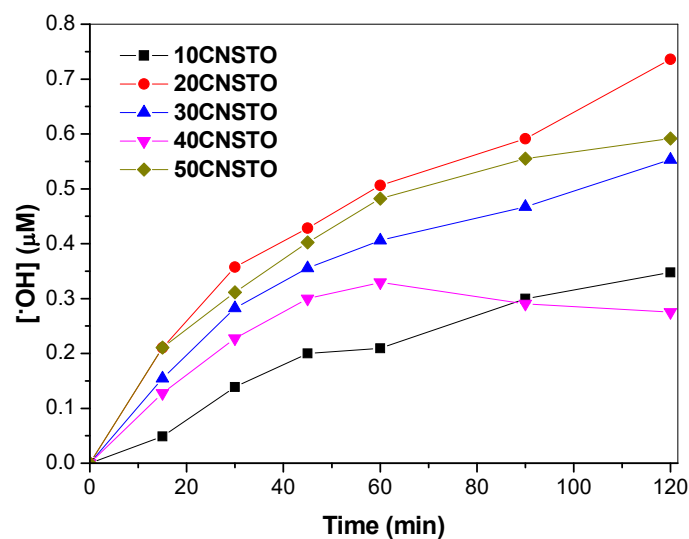
Figure 7. Kinetics of •OH formation for all composite catalysts based on OHTA fluorescence measurements.

## 2.2. Photocatalytic Activity

The photocatalytic activity of all catalysts towards the degradation of MB under UV-Vis and visible irradiation is presented in Figures 8 and 9, respectively. The degradation of MB in both cases followed first-order kinetics. As expected, the degradation kinetics under visible light irradiation was slower than under UV-Vis (simulated solar) irradiation. The apparent rate constants (k), the corresponding correlation coefficients (R^2) and half-lives ($t_{1/2}$) of all photocatalysts are shown in Table 3. According to the determined apparent rate constants, the photocatalytic activity under both UV-Vis and visible irradiation had the following trend: 20CNSTO > 30CNSTO > 40CNSTO > 50CNSTO ≈ 10CNSTO. The highest photocatalytic activity of the 20CNSTO catalyst is also verified by its ability to form •OH radicals. The corresponding apparent degradation rate constants trends for UV-Vis and visible light irradiation are presented in Figures 8 and 9. The initial increase in the degradation efficiency can be attributed to the increment of CN content which benefits charge transfer in the materials interface and causes greater response into the visible light region. The greater increment of g-C_3N_4 amount, though, decreases the effective heterointerfaces in the composites, which is unfavorable for the charge transfer [46,63] while the entrained decrease of STO, which has a higher oxidation potential valence band led to the decrease of •OH radicals formation.

Finally, the stability of the best catalyst (20CNSTO) was investigated for three consecutive photocatalytic cycles (Figure 10). The photocatalyst presented quite stable photocatalytic activity among the repeated cycles and about 95% of the initial degradation efficiency was maintained. This fact suggests that the 20CNSTO photocatalyst has good reusability. The slight decrease in the photocatalytic efficiencies could occur because of the accumulation of later stage products into the catalyst surface after the first catalytic cycle or because of small losses of catalyst during the recovery procedure due to the good dispersibility in the aqueous solution.
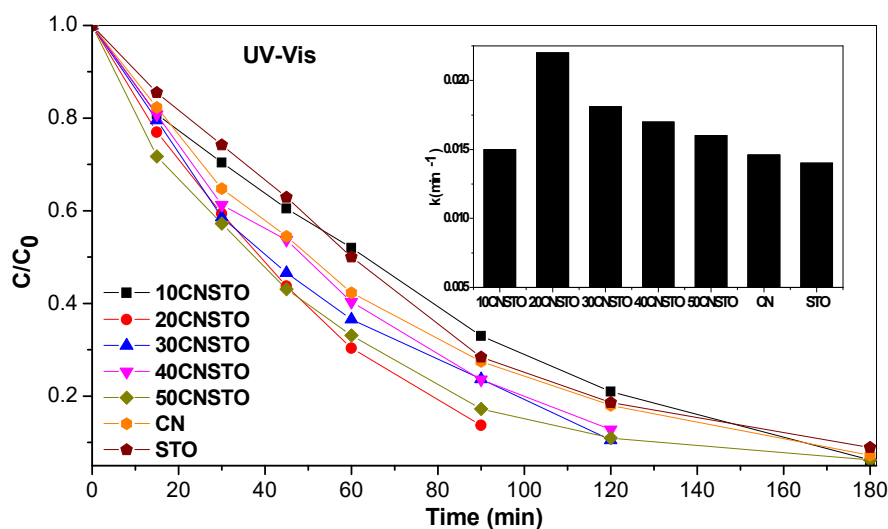
Figure 8. Degradation kinetics of MB under UV-Vis irradiation (C_{MB} = 5 mg L^{-1}, C_{cat} = 200 mg L^{-1}, I = 500 Wm^{-2}) and apparent rate constants (inset) for all studied photocatalysts.
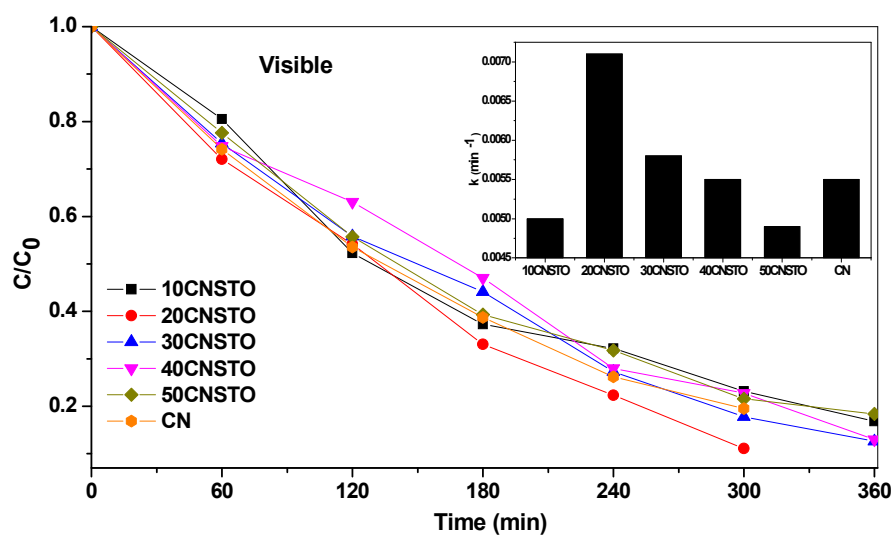
Figure 9. Degradation kinetics of MB under visible light irradiation (C_{MB} = 5 mg L^{-1}, C_{cat} = 200 mg L^{-1}, I = 500 Wm^{-2}) and apparent rate constants (inset) for all studied photocatalysts.

Table 3. Kinetic parameters (k, $t_{1/2}$, R^2) for the photocatalytic degradation of MB in the presence of the heterojunctions under simulated solar light (UV-Vis) and visible light irradiation (C_{MB} = 5 mg L^{-1}, C_{cat} = 200 mg L^{-1}, I = 500 Wm^{-2}).

Catalysts	UV-Vis			Visible		
	K (min^{-1})	$t_{1/2}$ (min)	R^2	K (min^{-1})	$t_{1/2}$ (min)	R^2
10CNSTO	0.0150	46.2	0.9804	0.0050	138.6	0.9690
20CNSTO	0.0220	31.5	0.9886	0.0071	97.6	0.9780
30CNSTO	0.0181	38.3	0.9885	0.0058	119.5	0.9893
40CNSTO	0.0170	40.8	0.9932	0.0055	126.0	0.9766
50CNSTO	0.0160	43.3	0.9797	0.0049	141.4	0.9942
STO	0.0140	49.5	0.9932	-	-	-
CN	0.0146	47.5	0.9996	0.0055	126.0	0.9986
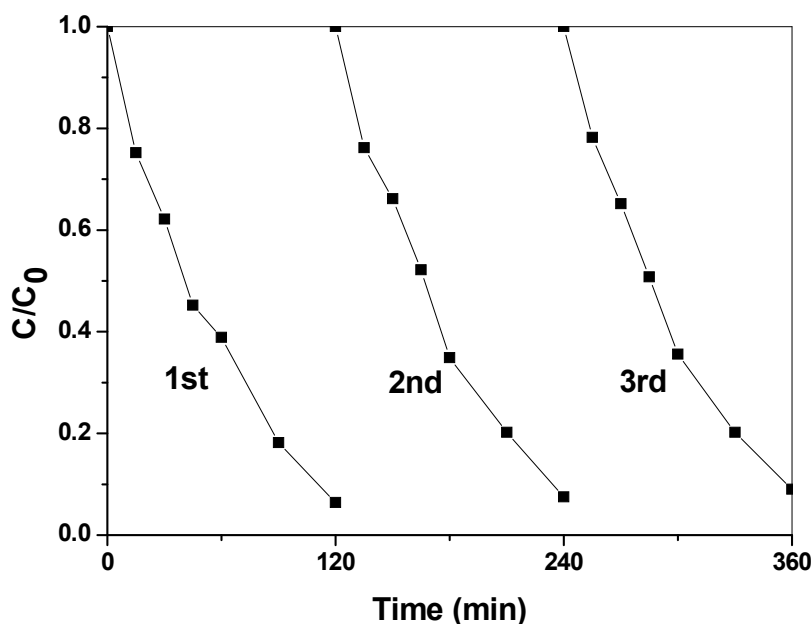
Figure 10. Reusability performance of TV450 20CNSTO photocatalyst for three consecutive catalytic cycles.

2.3. Mechanism Analysis

Generally, superoxide radicals ($O_2^{\bullet-}$), hydroxyl radicals ($OH^{\bullet}$) and the photogenerated holes (h^+) have important role in the photocatalytic process. To propose the proper photocatalytic mechanism for the activity of the photocatalyst, trapping experiments took place with the use of scavengers. The used scavengers were isopropanol (IPA), formic acid (FA), N_2, superoxide dismutase (SOD_{red}), acetonitrile/N_2, and sodium azide (NaN_3) as $OH^{\bullet}$, h^+, $O_2^{\bullet-}$, $OH^{\bullet}/O_2^{\bullet-}$ and ($OH^{\bullet} + {}^1O_2$) scavengers, respectively. The apparent rate constants (k) and the corresponding correlation coefficients (R^2) of 20CNSTO under the effect of each scavenger are presented in Table 4. The redox potentials of g-C_3N_4 (conduction band, CB = −1.4 eV vs. NHE (Normal Hydrogen Electrode), valence band VB = +1.3 eV vs. NHE) are more negative than those of $SrTiO_3$ (CB = −0.2 eV vs. NHE, VB = +3.0 eV vs. NHE) [52,63]. Based on the experimental results that are presented in Table 4, the classical Type II photocatalytic mechanism, i.e., the migration of electrons from the CB of CN to the CB of STO with concurrently migration of holes from VB of STO to VB of CN, is excluded. More specifically, in such mechanisms, the accumulated holes in the VB of g-C_3N_4 couldn't produce $^{\bullet}$OH from the oxidation-adsorbed water molecules or OH$^-$ ions because the VB potential was less positive than the redox potential $E^0_{(OH\bullet/H2O)}$ (+2.68 eV vs. NHE) and $E^0_{(OH^-/\bullet OH)}$ (+1.99 eV vs. NHE). However, according to the experimental results, $^{\bullet}$OH are indeed produced, as evidenced by OHTA fluorescence, as well as by the degradation rate decrease in the presence of IPA, NaN_3 and acetonitrile. In addition, the molecular O_2 could also not be photoreducted to $^{\bullet}$OH in the CB of $SrTiO_3$, as the CB potential was more positive than the redox potential $E^0_{(O_2/O_2^{\bullet-})}$ (−0.3 eV vs. NHE). Nevertheless, the decrease of the degradation rate in the presence of N_2 demonstrated the formation of $O_2^{\bullet-}$. Finally, the apparent rate constant value in the presence of acetonitrile/N_2 as a scavenger showed the oxidation of MB by the holes in the VB of $SrTiO_3$. As a result, a z-scheme mechanism is proposed for the photocatalytic activity of the composites. In the z-scheme mechanism, the photogenerated electrons in the CB of the STO will combine with the photogenerated holes in the VB of CN, while the accumulated holes the with high oxidation potential in the VB of STO and electrons with high reductive potential in the CB of CN could easily produce $^{\bullet}$OH and $O_2^{\bullet-}$, which participate in the oxidative degradation of MB. In conclusion, the results of the trapping experiments showed that $OH^{\bullet}$ and $O_2^{\bullet-}$ were the major oxidant species, followed by a minor contribution of $^1O_2$, and the generation of such species can only be rationalized by a z-scheme mechanism.

Table 4. Used scavengers for 20CNSTO along with the scavenged radicals, k (min^{-1}), % Δk and R^2.

		20CNSTO		
Scavengers	**Radicals Scavenge**	**k (min^{-1})**	**% Δk**	**R^2**
No scavenger	-	0.0220	0	0.9886
IPA	$OH^{\bullet}$	0.0148	32.7	0.9996
FA	h^+	0.0086	60.9	0.9803
N_2	$O_2^{\bullet-}$	0.0156	29.1	0.9773
Acetonitrile/N_2	$OH^{\bullet} / O_2^{\bullet-}$	0.0050	77.3	0.9052
SOD_{red}	$O_2^{\bullet-}$	0.0309	40.4	0.9936
NaN_3	$OH^{\bullet} + {}^1O_2$	0.0130	40.9	0.9814

3. Materials and Methods

3.1. Materials and Chemicals

Urea (99.5%) was obtained by Acros Organics (Geel, Belgium). Pure $SrTiO_3$ (STO) was purchased from Sigma–Aldrich (St. Louis, MO, USA). KBr ($\geq$ 99%, Sigma–Aldrich, St. Louis, MO, USA), $BaSO_4$ (NacalaiTesque, extra pure reagent, Kyoto, Japan), terephthalic acid (TA) (98%, Sigma-Aldrich, St. Louis, MO, USA) and NaOH (2×10^{-3} M, 99% Riedel-de Haen, Seelze, Germany) were also used in the present study. Finally, the used scavengers were isopropanol (IPA) (Ananlytical Reagent A.R., LAB-SCAN, Dublin, Ireland), formic acid (FA) (98-100%, Merck, Darmastadt Germany), N_2, acetonitrile (LC-MS grade, Fisher Chemical, Loughborough, Leics, UK)/N_2, superoxide dismutase (SOD) (SOD from Horseradish, Sigma-Aldrich, St. Louis, MO, USA) and sodium azide (NaN_3) ($\geq$99.5% Sigma-Aldrich, St. Louis, MO, USA). Double distilled water was used throughout all the experimental procedures.

3.2. Preparation of g-C_3N_4 and g-C_3N_4/$SrTiO_3$ Heterojunctions

For g-C_3N_4 synthesis, urea was preheated at 80 °C for 24 h in an alumina crucible and then calcined at 500 °C for 4 h with the heating rate of 10 °C /min [64,65]. The composite photocatalysts were prepared by a sonication mixing method. Appropriate stoichiometric amount of $SrTiO_3$ and g-C_3N_4 were suspended in double distilled water separately under sonication for 1 h. Then both solutions were mixed, and the whole solution was treated again under sonication for 90 min (Hielscher UP100H Teltow, Germany ultrasonic processor, Amplitude 85%). The as-prepared samples contained different g-C_3N_4 to $SrTiO_3$ amounts and had the following %wt content and code names (in brackets): 10% (10CNSTO), 20% (20CNSTO), 30% (30CNSTO), 40% (40CNSTO), 50% (50CNSTO) [57]. Also, for the comparison for the heterojunction oxides, g-C_3N_4 which had been sonicated for 1 h (CN) was also used.

3.3. Texture Characterization of the Heterojunctions

Crystallinity and phase identification of the photocatalytic materials were defined by powder X -ray diffraction (XRD) using a Bruker Advance D8 XRD instrument (Billerica, MA, USA), which generates monochromated Cu K_a (λ = 1.5418 Å) radiation with a continuous scanning rate in the range of 10 < 2θ < 90 in steps of 0.02° and rate 0.01 °θ/sec. The patterns were determined with the use of the Joint Committee on Powder Diffraction Standards (JCPDS) database. The results were studied with Rietvield refinement by a suitable computer program.

The N_2 adsorption–desorption isotherms at 77K were obtained by porosimetry using a Quantachrome Autosorb –1 instrument (Bounton Beach, FL, USA). All samples ($\approx$ 0.1 g) were degassed for 4h at 353 K for the elimination of any moisture and condensed volatiles. Brauner-Emmet-Teller (BET) method at relative pressure between 0.05–0.3 was used for the calculation of the specific surface area (SSA). The morphology of the photocatalysts was observed by scanning electron microscopy (SEM) by a JEOL JSM 5600 instrument (Tokyo, Japan).

Particle size measurements were carried out after 10 min of sonication with a Shimadzu SALD-2300 (Kyoto, Japan) laser diffraction particle size analyzer in dynamic light scattering (DLS) mode. The point-of-zero charge (PZC) of the materials was measured by the mass titration method, as reported elsewhere [66].

3.4. Fourier Transform. Infrared Spectroscopy (FT-IR)

The chemical structure of all heterojunctions was recorded by Fourier transform infrared spectroscopic (FT-IR) analysis. The analysis was carried out with an instrument by Thermo Scientific (Nicolet iS5) (Waltham, MA, USA). Spectral grade KBr ($\geq$99%, Sigma-Aldrich St. Louis, MO, USA) was used as a reference. The materials were ground with KBr in 1:3 ratio and made into pellets using an appropriate hydraulic press. The pellet was scanned at 0.964 cm^{-1} in the range $4000–400 \text{ cm}^{-1}$.

3.5. UV-Vis.-Diffuse Reflectance Measurements

The absorbance spectra of the $g\text{-}C_3N_4/SrTiO_3$ heterojunctions were obtained by a Shimadzu 2600 (Kyoto, Japan) spectrophotometer which was equipped with an ISR-2600 (Kyoto, Japan) integrating sphere at room temperature with $BaSO_4$ as reference sample in the range of 200–800 nm.

3.6. Photocatalytic Experiments and Analytical Methods

The photocatalytic experiments were conducted with Suntest XLS+ apparatus (Atlas Linsengericht, Germany) under UV-Vis irradiation (simulated solar light, $\lambda > 290$ nm). A xenon lamp (2.2 kW), jacked with special 290 nm cut-off glass filter, was the light source. During the experiments, the irradiation intensity was maintained at 500 W m^{-2}. Experiments under visible light irradiation ($\lambda > 400$ nm) were performed using LED flood lamps (LG SMD, LED, 45 pcs, Seoul, Korea) $2 \times 50 \text{ Wm}^{-2}$. The photocatalytic activity was tested against the degradation of methylene blue (MB).

For both UV-Vis and visible irradiation experiments, the photocatalysts were suspended in double distilled water by sonication for 10 min then transferred in an appropriate Pyrex glass reactor (250 mL) and stirred using a magnetic stirrer. An initial concentration of 5 mg L^{-1} of MB and 200 mg L^{-1} of photocatalyst was used in all experiments. Prior to irradiation, the suspension is magnetically stirred for 30 min in the dark to ensure substrate adsorption/desorption equilibrium established on the catalyst surface. During irradiation the temperature was kept at 23 ± 1 °C by water circulation in the jacket of the reactor and air-circulation.

3.7. Determination of $^{\bullet}$OH Radicals by Fluorescence Measurements

TA was used as a probe for the determination of hydroxyl radical formation rate. Aqueous solution contained of NaOH and TA (5×10^{-4} M) was prepared and then 20 mg of photocatalyst powder was suspended in the photocatalytic reactor and stirred for 30 min under UV-Vis irradiation. The irradiation conditions are described in the next paragraph. Portions of 5 mL of the suspension were collected at different time intervals and filtered with 0.45 µm membrane filter. A Shimadzu RF-5300PC (Kyoto, Japan) fluorescence spectrophotometer was used in order to measure the intensity of the fluorescence peak at 425 nm with 310 nm excitation, which is attributed to 2-hydroxyterephthalic acid (OHTA), and it is known to be proportional to the amount of $^{\bullet}$OH radicals produced. The concentration of $^{\bullet}$OH was calculated by a calibration curve plotting the fluorescence intensity of standard OHTA (TCI, > 98% TCI, Tokyo Chemical Industry, Tokyo, Japan) solutions.

4. Conclusions

Visible-light active $SrTiO_3/g\text{-}C_3N_4$ photocatalysts have been synthesized by a sonication mixing method. The optimum fortification level of $g\text{-}C_3N_4$ loading was 20%. All the prepared catalysts presented photocatalytic performance towards the decolorization of MB. Among them, the 20CNSTO material showed the best photocatalytic activity for the degradation of MB in both UV-Vis and visible

light irradiation. This fact is also proved because the 20CNSTO showed greater $^{\bullet}$OH formation ability of all the other heterojunctions. A z-scheme mechanism is proposed for the photocatalytic activity.

Author Contributions: Conceptualization and methodology, I.K., D.P. and T.A.; Formal analysis, P.-S.K., I.K., D.P.; Investigation, P.-S.K. and I.K.; Data curation, P.-S.K.; Writing—original draft preparation, P.-S.K. and I.K.; Writing—review and editing, P.-S.K., I.K. and D.P., T.A.; Validation and Visualization, P.-S.K.; Supervision, T.A. and I.K.

Conflicts of Interest: The authors declare no conflict of interest.

References

1. Serpone, N.; Emeline, A.V. Semiconductor photocatalysis —Past, present, and future outlook. *J. Phys. Chem. Lett.* **2012**, *3*, 673–677. [CrossRef] [PubMed]

2. Konstantinou, I.K.; Albanis, T.A. TiO$_2$-assisted photocatalytic degradation of azo dyes in aqueous solution: Kinetic and mechanistic investigations: A review. *Appl. Catal. B Environ.* **2004**, *49*, 1–14. [CrossRef]

3. Mohammad, N.; Arami, M. Degradation and toxicity reduction of textile wastewater using immobilized titania nanophotocatalysis. *J. Photochem. Photobiol. B Biol.* **2009**, *94*, 20–24.

4. Molinari, R.; Borgese, M.; Drioli, E.; Palmisano, L.; Schiavello, M. Hybrid processes coupling photocatalysis and membranes for degradation of organic pollutants in water. *Catal. Today* **2002**, *75*, 77–85.

5. Kato, H.; Sasaki, Y.; Shirakura, N.; Kudo, A. Synthesis of highly active rhodium-doped SrTiO$_3$ powders in Z-scheme systems for visible-light-driven photocatalytic overall water splitting. *J. Mater. Chem. A* **2013**, *1*, 12327–12333. [CrossRef]

6. Jia, Y.; Shen, S.; Wang, D.; Wang, X.; Shi, J.; Zhang, F.; Han, H.; Li, C. Composite Sr$_2$TiO$_4$/SrTiO$_3$ (La, Cr) heterojunction based photocatalyst for hydrogen production under visible light irradiation. *J. Mater. Chem. A* **2013**, *1*, 7905–7912. [CrossRef]

7. Maeda, K. Rhodium-Doped Barium Titanate Perovskite as a Stable p-Type Semiconductor Photocatalyst for Hydrogen Evolution under Visible Light. *ACS Appl. Mater. Interfaces* **2014**, *6*, 2167–2173. [CrossRef] [PubMed]

8. Alammar, T.; Hamm, I.; Wark, M.; Mudring, A.-V. Low-temperature route to metal titanate perovskite nanoparticles for photocatalytic applications. *Appl. Catal. B Environ.* **2015**, *178*, 20–28. [CrossRef]

9. Sulaeman, U.; Yin, S.; Sato, T. Solvothermal synthesis and photocatalytic properties of chromium-doped SrTiO$_3$ nanoparticles. *Appl. Catal. B Environ.* **2011**, *105*, 206–210. [CrossRef]

10. Yu, H.; Wang, J.; Yan, S.; Yu, T.; Zou, Z. Elements doping to expand the light response of SrTiO$_3$. *J. Photochem. Photobiol. A: Chem.* **2014**, *275*, 65–71. [CrossRef]

11. Wang, J.; Yin, S.; Komatsu, M.; Sato, T. Lanthanum and Nitrogen Co-Doped SrTiO$_3$ Powders as Visible Light Sensitive Photocatalyst. *J. Eur. Ceram. Soc.* **2005**, *25*, 3207–3212. [CrossRef]

12. Cao, T.; Li, Y.; Wang, C.; Shao, C.; Liu, Y. A facile in situ hydrothermal method to SrTiO$_3$/TiO$_2$ nanofiber heterostructures with high photocatalytic activity. *Langmuir* **2011**, *27*, 2946–2952. [CrossRef] [PubMed]

13. Van Benthem, K.; Elsässer, C.; French, R. Bulk electronic structure of SrTiO$_3$: Experiment and theory. *J. Appl. Phys.* **2001**, *90*, 6156–6164. [CrossRef]

14. Sayama, K.; Mukasa, K.; Abe, R.; Abe, Y.; Arakawa, H. A new photocatalytic water splitting system under visible light irradiation mimicking a Z-scheme mechanism in photosynthesis. *J. Photochem. Photobiol. A Chem.* **2002**, *148*, 71–77. [CrossRef]

15. Jiang, Z.; Xiao, T.; Kuznetsov, V.L.; Edwards, P.P. Turning carbon dioxide into fuel. *Philos. Trans. R. Soc. Lond. A* **2010**, *368*, 3343–3364. [CrossRef] [PubMed]

16. Konta, R.; Ishii, T.; Kato, H.; Kudo, A. Photocatalytic Activities of Noble Metal Ion Doped SrTiO$_3$ under Visible Light Irradiation. *J. Phys. Chem. B* **2004**, *108*, 8992–8995. [CrossRef]

17. Puangpetch, T.; Chavadej, S.; Sreethawong, T. Hydrogen production over Au-loaded mesoporous-assembled SrTiO$_3$ nanocrystal photocatalyst: Effects of molecular structure and chemical properties of hole scavengers. *Energy Convers. Manag.* **2011**, *52*, 2256–2261. [CrossRef]

18. Kappadan, S.; Gebreab, T.W.; Thomas, S.; Kalarikkal, N. Tetragonal BaTiO$_3$ nanoparticles: An efficient photocatalyst for the degradation of organic pollutants. *Mat. Sci. Semicond. Proc.* **2016**, *51*, 42–47. [CrossRef]

19. Liu, J.; Wang, L.; Liu, J.; Wang, T.; Qu, W.; Li, Z. DFT study on electronic structures and optical absorption properties of C, S cation- doped SrTiO₃. *Cent. Eur. J. Phys.* **2009**, *7*, 762–767. [CrossRef]

20. Zhang, J.; Bang, J.H.; Tang, C.; Kamat Pr., V. Tailored TiO₂-SrTiO₃ Heterostructure Nanotube Arrays for Improved Photoelectrochemical Performance. *ACS Nano* **2010**, *4*, 387–395. [CrossRef] [PubMed]

21. Boumaza, S.; Boudjemaa, A.; Bouguelia, A.; Bouarab, R.; Trari, M. Visible light induced hydrogen evolution on new hetero-system ZnFe₂O₄/SrTiO₃. *Appl. Energy* **2010**, *87*, 2230–2236. [CrossRef]

22. Zhao, Z.; Sun, Y.; Dong, F. Graphitic carbon nitride based nanocomposites: A review. *Nanoscale* **2014**, *7*, 15–37. [CrossRef] [PubMed]

23. Ong, W.J.; Tan, L.L.; Ng, Y.H.; Yong, S.T.; Chai, S.P. Graphitic carbon nitride(g-C₃N₄)-Based photocatalysts for artificial photosynthesis and environmental remediation: Are we a step closer to achieving sustainability. *Chem. Rev.* **2016**, *116*, 7159–7329. [CrossRef] [PubMed]

24. Zhu, J.; Xiao, P.; Li, H.; Carabineiro, S.A.C. Graphitic carbon nitride: Synthesis, properties, and applications in catalysis. *ACS Appl. Mater. Interfaces* **2014**, *6*, 16449–16465. [CrossRef] [PubMed]

25. Ou, H.; Lin, L.; Zheng, Y.; Yang, P.; Fang, Y.; Wang, X. Tri-s-triazine-based crystalline carbon nitride nanosheets for an improved hydrogen evolution. *Adv. Mater.* **2017**, *29*, 1700008. [CrossRef] [PubMed]

26. Yang, P.; Ou, H.; Fang, Y.; Wang, X. A facile steam reforming strategy to delaminate layered carbon nitride semiconductors for photoredox catalysis. *Angew. Chem. Int. Ed.* **2017**, *56*, 3992–3996. [CrossRef] [PubMed]

27. Wang, H.; Yuan, X.; Wu, Y.; Huang, H.; Peng, X.; Zeng, G.; Zhong, H.; Liang, J.; Ren, M.M. Graphene-based materials: Fabrication, characterization and application for the decontamination of wastewater and waste gas and hydrogen storage/generation. *Adv. Colloid Interface Sci.* **2013**, *195–196*, 19–40. [CrossRef] [PubMed]

28. Song, X.; Hu, J.; Zeng, H. Two-dimensional semiconductors: Recent progress and future perspectives. *J. Mater. Chem. C* **2013**, *1*, 2952–2969. [CrossRef]

29. Wang, X.; Sun, G.; Li, N.; Chen, P. Quantum dots derived from two-dimensional materials and their applications for catalysis and energy. *Chem. Soc. Rev.* **2016**, *45*, 2239–2262. [CrossRef] [PubMed]

30. Mamba, G.; Mishra, A.K. Graphitic carbon nitride (g-C₃N₄) nano composites: A new and exciting generation of visible light driven photocatalysts for environmental pollution remediation. *Appl. Catal. B Environ.* **2016**, *198*, 347–377. [CrossRef]

31. Wu, Z.; Zhong, H.; Yuan, X.; Wang, H. Adsorptive removal of methylene blue by rhamnolipid-functionalized graphene oxide from wastewater. *Water Res.* **2014**, *67*, 330–344. [CrossRef] [PubMed]

32. Wu, Z.; Yuan, X.; Zhong, H.; Wang, H.; Zeng, G.; Chen, X.; Wang, H.; Zhang, L.; Shao, J. Enhanced adsorptive removal of p-nitrophenol from water by aluminum metal-organic framework/reduced graphene oxide composite. *Sci. Rep.* **2016**, *6*, 25638. [CrossRef] [PubMed]

33. Xu, M.; Liang, T.; Shi, M.; Chen, H. Graphene-like two-dimensional materials. *Chem. Rev.* **2013**, *113*, 3766–3798. [CrossRef] [PubMed]

34. Wen, P.; Gong, P.; Sun, J.; Wang, J.; Yang, S. Design and synthesis of Ni-MOF/CNT composites and rGO/carbon nitride composites for an asymmetric supercapacitor with high energy and power density. *J. Mater. Chem. A: Chem.* **2015**, *3*, 13874–13883. [CrossRef]

35. Dyjak, S.; Kicinski, W.; Huczko, A. Thermite-driven melamine condensation to $C_xN_yH_z$ graphitic ternary polymers: Towards an instant, large-scale synthesis of g-C₃N₄. *J. Mater. Chem. A.* **2015**, *3*, 9621–9631. [CrossRef]

36. Zhang, X.-S.; Tian, K.; Hu, J.-Y.; Jiang, H. Significant enhancement of photoreactivity of graphitic carbon nitride catalysts under acidic conditions and the underlying H⁺-mediated mechanism. *Chemosphere* **2015**, *141*, 127–133. [CrossRef] [PubMed]

37. Wang, Z.; Guan, W.; Sun, Y.; Dong, F.; Zhou, Y.; Ho, W.-K. Water-assisted production of honeycomb-like g-C₃N₄ with ultralong carrier lifetime and outstanding photocatalytic activity. *Nanoscale* **2015**, *7*, 2471–2479. [CrossRef] [PubMed]

38. Chen, D.; Wang, K.; Hong, W.; Zong, R.; Yao, W.; Zhu, Y. Visible light photoactivity enhancement via CuTCPP hybridized g-C₃N₄ nanocomposite. *Appl. Catal. B Environ.* **2015**, *166–167*, 366–373. [CrossRef]

39. Liu, G.; Niu, P.; Sun, C.; Smith, S.C.; Chen, Z.; Lu, G.Q.; Cheng, H.M. Unique electronic structure induced high photoreactivity of sulfur-doped graphitic C₃N₄. *J. Am. Chem. Soc.* **2010**, *132*, 11642–11648. [CrossRef] [PubMed]

40. Yan, S.-C.; Li, Z.-S.; Zou, Z.-G. Photodegradation of Rhodamine B and methyl orange over boron-doped g-C3N4 under visible light irradiation. *Langmuir* **2010**, *26*, 3894–3901. [CrossRef] [PubMed]

41. Zhang, Y.-J.; Mori, T.; Ye, J.-H.; Antonietti, M. Phosphorus-doped carbon nitride solid: Enhanced electrical conductivity and photocurrent generation. *J. Am. Chem. Soc.* **2010**, *132*, 6294–6295. [CrossRef] [PubMed]

42. Yue, B.; Li, Q.-Y.; Iwai, H.; Kako, T.; Ye, J.-H. Hydrogen production using zinc-doped carbon nitride catalyst irradiated with visible light. *Sci. Technol. Adv. Mater.* **2011**, *12*, 034401. [CrossRef] [PubMed]

43. Mitoraj, D.; Kisch, H. The nature of nitrogen-modified titanium dioxide photocatalysts active in visible light. *Angew. Chem. Int. Ed. Engl.* **2008**, *47*, 9975–9978. [CrossRef] [PubMed]

44. Li, Q.Y.; Yue, B.; Iwai, H.; Kako, T.; Ye, J.H. Carbon nitride polymers sensitized with N-doped tantalic acid for visible light- Induced photocatalytic hydrogen evolution. *J. Phys. Chem. C* **2010**, *114*, 4100–4105. [CrossRef]

45. Rakibuddin, Md.; Kim, H.; Khan, M.E. Graphite-like carbon nitride (C_3N_4) modified N-doped LaTiO$_3$ nanocomposite for higher visible light photocatalytic and photo-electrochemical performance. *Appl. Surf. Sci.* **2018**, *452*, 400–412. [CrossRef]

46. Wu, Y.; Wang, H.; Tu, W.; Liu, Y.; Tan, Y.Z.; Yuan, X.; Chew, J.W. Quasi-polymeric construction of stable perovskite-type LaFeO$_3$/g-C$_3$N$_4$ heterostructured photocatalyst for improved Z-scheme photocatalytic activity via solid p-n heterojunction interfacial effect. *J. Hazard. Mater.* **2018**, *347*, 412–422. [CrossRef] [PubMed]

47. Kumar, A.; Schuerings, C.; Kumar, S.; Kumar, A.; Krishnan, V. Perovskite-structured CaTiO$_3$ coupled with g-C$_3$N$_4$ as a heterojunction photocatalyst for organic pollutant degradation. *Beilstein J. Nanotechnol.* **2018**, *9*, 671–685. [CrossRef] [PubMed]

48. Kumar, S.; Tonda, S.; Baruah, A.; Kumar, B.; Shanker, V. Synthesis of novel and stable g-C$_3$N$_4$/N-doped SrTiO$_3$ hybrid nanocomposites with improved photocurrent and photocatalytic activity under visible light irradiation. *Dalton Trans.* **2014**, *43*, 16105–16114. [CrossRef] [PubMed]

49. Luo, J.; Zhou, X.; Ning, X.; Zhan, L.; Chen, J.; Li, Z. Constructing a direct Z-scheme La$_2$NiO$_4$/g-C$_3$N$_4$ hybrid photocatalyst with boosted visible light photocatalytic activity. *Sep. Purif. Technol.* **2018**, *201*, 327–335. [CrossRef]

50. Chen, X.; Tan, P.; Zhou, B.; Dong, H.; Pan, J.; Xiong, X. A green and facile strategy for preparation of novel and stable Cr-doped SrTiO$_3$/g-C$_3$N$_4$ hybrid nanocomposites with enhanced visible light photocatalytic activity. *J. Alloys Compd.* **2015**, *647*, 456–462. [CrossRef]

51. Xu, X.; Liu, G.; Randorn, C.; Irvine, J.T.S. g-C$_3$N$_4$ coated SrTiO$_3$ as an efficient photocatalyst for H$_2$ production in aqueous solution under visible light irradiation. *Int. J. Hydrog. Energy* **2011**, *36*, 13501–13507. [CrossRef]

52. Kang, H.W.; Lim, S.N.; Song, D.; Park, S.B. Organic-inorganic composite of g-C$_3$N$_4$-SrTiO$_3$: Rh photocatalyst for improved H$_2$ evolution under visible light irradiation. *Int. J. Hydrog. Energy* **2012**, *37*, 11602–11610. [CrossRef]

53. Rietveld, H.M. Line profiles of neutron powder-diffraction peaks for structure refinement. *Acta Cryst.* **1967**, *22*, 151–152. [CrossRef]

54. Mittemeijer, E.J.; Welzel, U. The "state of the art" of the diffraction analysis of crystallite size and lattice strain. *Z. Kristallogr.* **2008**, *223*, 552–560. [CrossRef]

55. Hall, W.H. X-ray line broadening in metals. *Proc. Philos. Soc. Lond.* **1949**, *62*, 741–743. [CrossRef]

56. Williamson, G.K.; Hall, W.H. X-ray line broadening from filed aluminium and wolfram. *Acta Metall.* **1953**, *1*, 22–31. [CrossRef]

57. Acharya, S.; Mansingh, S.; Parida, K.M. The enhanced photocatalytic activity of g-C$_3$N$_4$-LaFeO$_3$ for water reduction reaction through mediator free Z-scheme mechanism. *Inorg. Chem. Fron.* **2017**, *4*, 1022–1032. [CrossRef]

58. Xian, T.; Yang, H.; Di, L.J.; Dai, J.F. Enhanced photocatalytic activity of BaTiO$_3$@g-C$_3$N$_4$ for the degradation of methyl orange under simulated sunlight irradiation. *J. Alloys Compd.* **2015**, *622*, 1098–1104. [CrossRef]

59. Thommes, M.; Kaneko, K.; Neimark, A.V.; Olivier, J.P.; Rodriguez-Reinoso, F.; Rouquerol, J.; Sing, K.S.W. Physisorption of gases, with special reference to the evaluation of surface area and pore size distribution (IUPAC Technical Report). *Pure Appl. Chem.* **2015**, *87*, 1051–1069. [CrossRef]

60. Jia, A.; Liang, X.; Su, Z.; Zhu, T.; Liu, S. Synthesis and the effect of calcination temperature on the physical–chemical properties and photocatalytic activities of Ni, La codoped SrTiO$_3$. *J. Hazard. Mater.* **2010**, *178*, 233–242. [CrossRef] [PubMed]

61. Wu, Z.; Zhang, Y.; Wang, X.; Zou, Z. Ag@SrTiO$_3$ nanocomposite for super photocatalytic degradation of organic dye and catalytic reduction of 4-nitrophenol. *New J. Chem.* **2017**, *41*, 5678–5687. [CrossRef]

62.　Yang, M.; Jin, X.-Q. Improvement of visible light-induced photocatalytic performance by Cr-doped SrTiO$_3$−carbon nitride intercalation compound (CNIC) composite. *J. Cent. South Univ.* **2016**, *23*, 310–316. [CrossRef]

63.　Sun, L.; Qi, Y.; Jia, C.J.; Jin, Z.; Fan, W. Enhanced visible-light photocatalytic activity of g-C$_3$N$_4$/Zn$_2$GeO$_4$ heterojunctions with effective interfaces based on band match. *Nanoscale* **2014**, *6*, 2649–2659. [CrossRef] [PubMed]

64.　Li, Y.; Wang, J.; Yang, Y.; Zhang, Y.; He, D.; An, Q.; Cao, G. Seed-induced growing various TiO$_2$ nanostructures on g-C$_3$N$_4$ nanosheets with much enhanced photocatalytic activity under visible light. *J. Hazard. Mater.* **2015**, *292*, 79–89. [CrossRef] [PubMed]

65.　Chen, X.; Li, H.; Wu, Y.; Wu, H.; Wu, L.; Tan, P.; Pan, J.; Xiong, X. Facile fabrication of novel porous graphitic carbon nitride/copper sulfide nanocomposites with enhanced visible light driven photocatalytic performance. *J. Colloid Interface Sci.* **2016**, *476*, 132–143. [CrossRef] [PubMed]

66.　Bourikas, K.; Vakros, J.; Kordulis, C.; Lycourghiotis, A. Potentiometric Mass Titrations: Experimental and Theoretical Establishment of a New Technique for Determining the Point of Zero Charge (PZC) of Metal (Hydr)Oxides. *J. Phys. Chem. B* **2003**, *107*, 9441–9451. [CrossRef]